GRAIL gravity constraints on the vertical and lateral density structure of the lunar crust

Jonathan Besserer[1], Francis Nimmo[1], Mark A. Wieczorek[2], Renee C. Weber[3], Walter S. Kiefer[4], Patrick J. McGovern[4], Jeffrey C. Andrews-Hanna[5], David E. Smith[6], and Maria T. Zuber[6]

[1]Department of Earth and Planetary Sciences, University of California, Santa Cruz, California, USA, [2]Institut de Physique du Globe de Paris, Sorbonne Paris Cité, Université Paris Diderot, Paris, France, [3]NASA Marshall Space Flight Center, Huntsville, Alabama, USA, [4]Center for Lunar Science and Exploration, Lunar and Planetary Institute, Houston, Texas, USA, [5]Department of Geophysics and Center for Space Resources, Colorado School of Mines, Golden, Colorado, USA, [6]Department of Earth, Atmospheric and Planetary Sciences, Massachusetts Institute of Technology, Cambridge, Massachusetts, USA

Abstract We analyzed data from the Gravity Recovery and Interior Laboratory (GRAIL) mission using a localized admittance approach to map out spatial variations in the vertical density structure of the lunar crust. Mare regions are characterized by a distinct decrease in density with depth, while the farside is characterized by an increase in density with depth at an average gradient of ∼35 kg m^{-3} km^{-1} and typical surface porosities of at least 20%. The Apollo 12 and 14 landing site region has a similar density structure to the farside, permitting a comparison with seismic velocity profiles. The interior of the South Pole-Aitken (SP-A) impact basin appears distinct with a near-surface low-density (porous) layer 2–3 times thinner than the rest of the farside. This result suggests that redistribution of material during the large SP-A impact likely played a major role in sculpting the lunar crust.

1. Introduction

Since the acquisition of the last lunar seismic data, almost 40 years ago, the main way of investigating lunar crustal structure has been through gravity analysis via spacecraft tracking data from missions such as Clementine [*Zuber et al.*, 1994], Lunar Prospector [*Konopliv et al.*, 1998], SELENE [*Goossens et al.*, 2011], and Lunar Reconnaissance Orbiter [*Mazarico et al.*, 2012]. More recently, the Gravity Recovery and Interior Laboratory (GRAIL) mission has acquired highly accurate observations through the use of a pair of coorbiting spacecraft [*Zuber and Russell*, 2014], and in this manner, the lunar gravity field has been measured to a much higher accuracy and resolution than previous missions both over the nearside and the farside of our satellite [*Zuber et al.*, 2013; *Han*, 2013; *Konopliv et al.*, 2013; *Lemoine et al.*, 2013; *Konopliv et al.*, 2014; *Lemoine et al.*, 2014]. The lunar anorthositic crust has been found to be much less dense than previously thought, and GRAIL data has revealed a significant bulk crustal porosity of ∼12% [*Wieczorek et al.*, 2013a].

Further analysis of GRAIL data has shown a general density increase (i.e., porosity decrease) with depth [*Wieczorek et al.*, 2013b; *Han et al.*, 2014]. However, regional variations in the density profile, that is the 3-D crustal density/porosity distribution, are currently poorly known. These vertical and lateral variations are key to interpret the Apollo heat flux measurements [*Langseth et al.*, 1976; *Rasmussen and Warren*, 1985; *Siegler and Smrekar*, 2014] to constrain lunar thermal evolution models [e.g., *Ziethe et al.*, 2009; *Laneuville et al.*, 2013] and are also relevant to seismic velocity profiles inferred from the Apollo data [e.g., *Lognonné et al.*, 2003; *Khan et al.*, 2013]. To investigate the regional variations of the density stratification, we performed a localized admittance analysis using high-resolution GRAIL data.

2. Methodology

We used spherical harmonic coefficients of the Moon's gravity (*Lemoine et al.* [2014] model GRGM900B), topography expanded in the same principal axis coordinate frame, and gravitational contribution from the surface topography (Bouguer correction) [*Wieczorek et al.*, 2013a] up to spherical harmonic degree $\ell = 550$. The gravity data were derived from the GRAIL nominal and extended missions' tracking data; the topography data were derived from the Lunar Orbiter Laser Altimeter data [*Smith et al.*, 2010] (see Table S1 in the supporting information). A localized, multitaper spherical harmonic analysis [*Wieczorek and Simons*, 2005,

2007] was performed over spherical cap regions 15° in radius. The latter were centered at 400 grid nodes distributed in a quasi-equal area fashion, yielding a grid spatial resolution of ~290 km. A combination of 30 optimal filters (spherical Slepian functions) of large spectral bandwidth ($L = 58$; Shannon number of ~59) was used to localize the gravity and topography-induced gravity data [*Wieczorek and Simons*, 2005, 2007; *Simons et al.*, 2006; *Dahlen and Simons*, 2008]. The resulting fields were expanded in spherical harmonics, from which the effective density ρ_{eff} (which compares the observed gravity to that predicted from the topography) as a function of ℓ was calculated (see section S4 in the supporting information):

$$\rho_{eff}(\ell) = \frac{S_{gb}(\ell)}{S_{bb}(\ell)}, \tag{1}$$

where g refers to the observed (free-air) gravity and b to the Bouguer correction per unit density [*Wieczorek et al.*, 2013a], respectively. S_{fg} is the cross-power spectrum of two functions f and g on the sphere. Equation (1) is similar to the usual admittance formula, for which b would be replaced by h, the surface topography.

The resulting global effective density spectrum shows a decrease in density with increasing ℓ (see below). Since smaller degrees sample greater depths, this implies that density generally increases with depth [*Wieczorek et al.*, 2013b; *Han et al.*, 2014]. Note that $\rho_{eff}(\ell)$ would be constant if the crustal density was constant with depth. Hence, these spectra were fit to two kinds of theoretical spectra [equations (S7) and (S10)] assuming, respectively, either a linear or an exponential density profile in the crust (see sections S1 and S2 in the supporting information). Such a multitaper moving window combined with a best fit approach is similar to the procedure of *Lewis and Simons* [2012]. The fits were performed for the high-degree portion of the data ($250 \leq \ell \leq 550$) in order to avoid the effects of flexure and/or crustal thickness variations at lower degrees. Note that our use of high-degree data naturally removes the mascons' signature which could otherwise bias the results. Our method is therefore mostly sensitive to the shallow density structure of the crust (typically depths < 20 km). The best fit parameters describing the theoretical spectra were derived using a grid search. The uncertainties in these parameters were estimated by means of Monte Carlo simulations under the assumption that the nonunity correlation between predicted and observed gravity is a consequence of geologic "noise" resulting in gravity contributions uncorrelated with the topography (see section S5 in the supporting information).

3. Results

Figure 1 shows the spatial distribution of the best fit linear density gradient a (Figure 1a) and associated surface density ρ_{surf} (Figure 1b). The mare regions exhibit high surface densities and a distinct decrease in density with depth. This is to be expected if high-density mare basalts overlie lower density anorthositic crustal material. Figure 1a shows that this model can discriminate between mare and nonmare regions. In detail our assumption that subsurface density interfaces are parallel to the surface (see section S1 in the supporting information) may not be appropriate for mare regions. Nevertheless, it is worth noting that in the degree range we consider ($\ell = 250-550$) that the correlation is very close to unity (see below) over the mare regions, implying that buried interfaces that are uncorrelated with surface topography do not contribute significantly to the gravity. Conversely, a negative correlation is retrieved at very low degrees. As the mare regions clearly have characteristics distinct from nonmare regions, our methodology may thus provide a way of identifying regions of buried (crypto-)mare [*Antonenko et al.*, 1995]. Some mare have similar spectral characteristics as the highlands, probably because these features are too small, either laterally or vertically, to be resolved; note, however, the faint signal associated with the small mare region over the southwestern rim of Apollo crater (Figure 1a).

In contrast, most of the farside is characterized by an increase in density with depth, with typical gradients of $20 - 45$ kg m^{-3} km^{-1}. The Apollo 12 and 14 landing sites, which are, respectively, covered and surrounded by mare basalts, lie in a region that resembles the farside in terms of vertical density structure. The Apollo 15 and 17 sites, where the only lunar heat flow measurements were carried out [*Langseth et al.*, 1976], lie in typical mare-bearing regions with negative values of a.

The typical high mare surface density (>2600 kg m^{-3}) presumably reflects a combination of compositional (the mare have higher grain densities) and porosity (the mare are relatively uncratered) effects. The general density increase with depth that characterizes the farside highlands presumably reflects a decrease
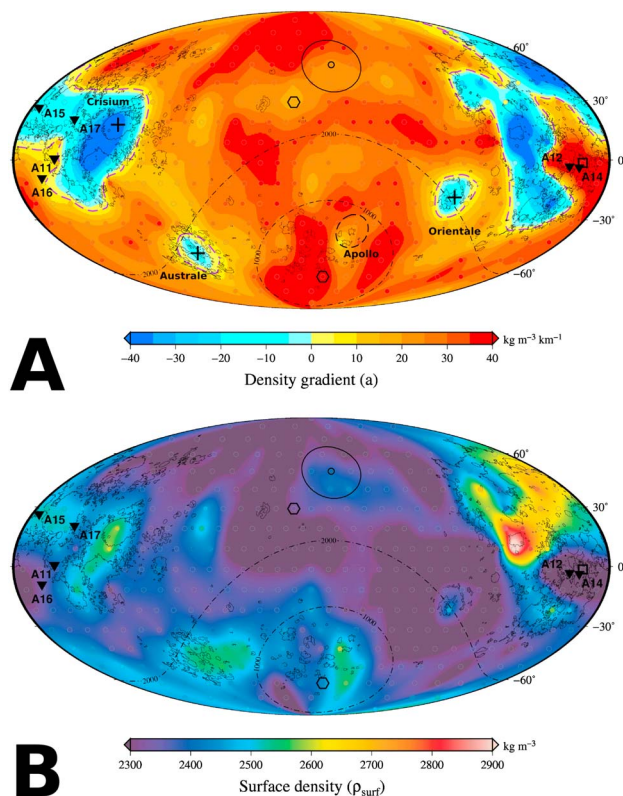
Figure 1. Density structure inferred from a linear model profile ($\rho(z) = \rho_{surf} + az$; see equation (S7) for the corresponding effective density spectrum). (a) Best fit shallow crustal density gradient a. (b) Corresponding map of ρ_{surf}. Note that ρ_{surf} is typically lower than the bulk crustal density [*Wieczorek et al.*, 2013a]. Triangles depict the location of the six Apollo landing sites. The two dash-dotted lines indicate distances of 1000 and 2000 km from the center of the South Pole-Aitken impact basin. Dashed circle indicates the Apollo crater. The faint, gray circles locate the centers of the regions of interest (ROIs) used in this study, characterized by a single value of each fitting parameters (here a and ρ_{surf})—this depicts the spatial resolution employed (∼290 km). Thin lines outline the maria (three main mare regions are indicated on Figure 1a). The thick line shows the radial extent (15°) of the employed localization window. The two hexagons and the square indicate locations depicted in Figures 3 and 4, respectively. The purple dashed lines (Figure 1a) depict the limit between regions with a smaller/greater than 5 kg m^{-3} km^{-1}. Data are presented in an equatorial view, centered on the farside—Mollweide equal area projection.

in porosity with depth [*Wieczorek et al.*, 2013a; *Han et al.*, 2014], though a more mafic lower crust might contribute to this general gradient.

In contrast to the nearside mare-bearing regions, the farside and South Pole-Aitken (SP-A) basin are characterized by a density increase with depth. In the following, regions with gradients less than +5 kg m^{-3} km^{-1} (corresponding to our finite grid search step) were excluded (purple dashed line in Figure 1a). We next assume what is likely to be a more realistic density profile for the nonmare regions of the Moon. For these regions, we used an exponential density profile given by $\rho = \rho_{surf} + \Delta\rho(1 - e^{-z/d})$, where z is depth, d is an e-folding depth scale, and $\Delta\rho$ is the density contrast between fractured surface materials and deeper unfractured rocks, i.e., $\rho_0 = \rho_{surf} + \Delta\rho$. For each location, the local, window-averaged value of the expected value of ρ_0 was calculated from the surface grain density model of *Huang and Wieczorek* [2012] and Lunar Prospector iron and titanium abundances, though our results are relatively insensitive to the assumed value (see section S6 in the supporting information). For the farside highlands as a whole (see Figure S3), the best fit density profile characteristics are $d = 9.0^{+2.2}_{-1.8}$ km and $\rho_{surf} = 2223^{+44}_{-54}$ kg m^{-3} (see section S5 for calculation of the uncertainties), corresponding to a typical surface porosity of 22–26% (the average grain density being 2917 kg m^{-3}); the equivalent density gradient with a linear model is $a \approx 35$ kg m^{-3} km^{-1}. Bulk density laboratory measurements on feldspathic

Apollo samples and lunar meteorites are commonly in the range 2400–2700 kg m^{-3}, although a small percentage of less dense rocks also exist [*Kiefer et al.*, 2012]. These densities are consistent with the densities observed over much of the Moon's highland crust (Figure 1) but do not explain the lowest densities seen in this map. One possibility is that the existing sample suite does not fully reflect the range of material properties of lunar surface rocks. An alternative is that a portion of the porosity in the Moon's uppermost crust occurs in large-scale void space, which would not be sampled in hand-specimen size rocks.

Figure 2 shows the spatial distribution of the e-folding depth scale d. The most striking result is that the interior of the SP-A impact basin region has a significantly thinner low-density (porous) layer than the rest of the farside, with $d = 5$–10 km, instead of 15–25 km. Recall that, although our spatial resolution is controlled by the 15° window radius, the long-wavelength spatial patterns in Figures 1–2 were obtained from short-wavelength ($\ell = 250$–550) gravity and topography data.

The dichotomy between the SP-A region and the remaining farside is further illustrated in Figure 3, which shows end-member examples of effective density spectra for these two regions. For these two particular
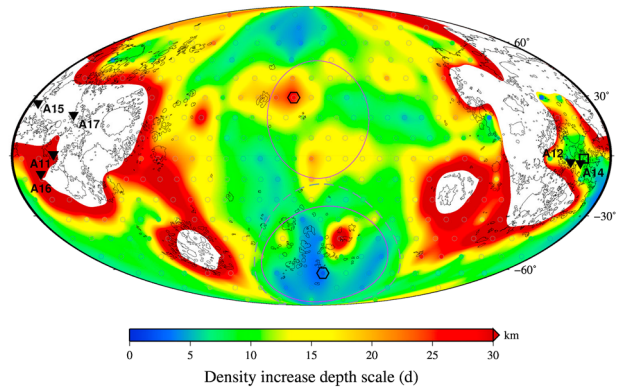
Figure 2. Spatial distribution of the best fitting depth scale d for a model with an exponential density profile ($\rho(z) = \rho_{surf} + \Delta\rho(1 - e^{-z/d})$; see also equation (S10)). General image format is the same as in Figure 1. The masked (white) areas corresponds to $a < 5$ kg m^{-3}km^{-1} in Figure 1a. The two purple circles depict the regions (SP-A versus non-SP-A farside) for which a Monte Carlo statistical analysis was performed (see text). The gray, dashed line corresponds to the best fit ellipse (outer topography [*Garrick-Bethell and Zuber*, 2009]) for SP-A.

regions of interest, we obtained $\rho_{surf} \leq$ 2206 kg m^{-3} with $d = 2.3^{+1.1}_{-0.2}$ km for the region within SP-A, and $\rho_{surf} = 2308^{+34}_{-40}$ kg m^{-3} with $d = 28.4^{+19.8}_{-9.3}$ km for the non-SP-A region. The corresponding best fit spectra are displayed, together with the local correlation. Figure 3 also shows the associated misfit maps in the $\Delta\rho - d$ parameter space. The SP-A/non-SP-A farside dichotomy (Figures 2–3) appears to be statistically significant, as can be seen from a Monte Carlo analysis (see section S5 in the supporting information) over two typical, broad areas (see Figure 2 for their location). The differences between SP-A and the rest of the farside are robust to details of data analysis and fitting, and to the theoretical density model employed
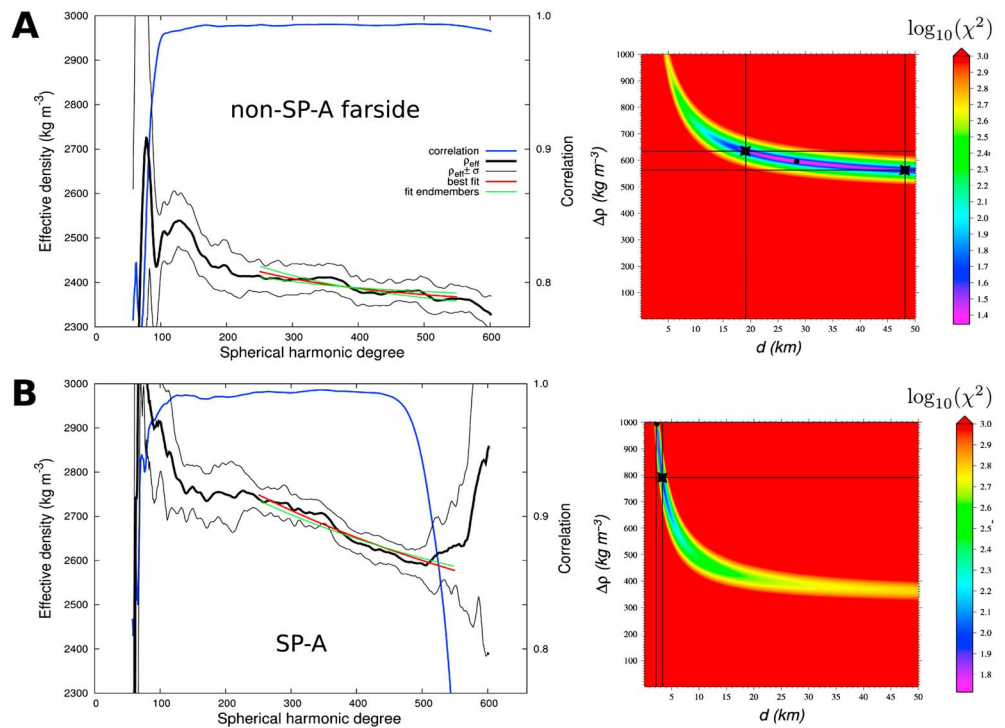

Figure 3. Observed and modeled effective density spectra for two end-member regions on the farside. Corresponding ROIs are located (Figures 1 and 2) (b) inside and (a) external to SP-A. Note the generally lower effective density of the non-SP-A spectrum. Data are displayed over the degree range $L < \ell < 660 - L$, where $L = 58$ is the filter's spectral bandwidth. The various lines depict the following: observed effective density spectra (thick black line) with associated ±1 standard deviation levels, best fit theoretical spectra assuming exponentially varying density (red), and examples of end-member fits (green). The correlation between the observed gravity and the gravity predicted from topography is also displayed (blue). The correlation is typically close to unity, except for $\ell > 500$ in Figure 3—this is due to reduced signal-to-noise owing to the higher spacecraft altitude in this region. Associated misfit maps in the $\Delta\rho - d$ parameter space are displayed in the right column: value of the chi-square (color scale) and admissible parameters' range (see section S5 in the supporting information) (black lines); dots mark the best fit location, whereas stars mark the location of end-member spectra.
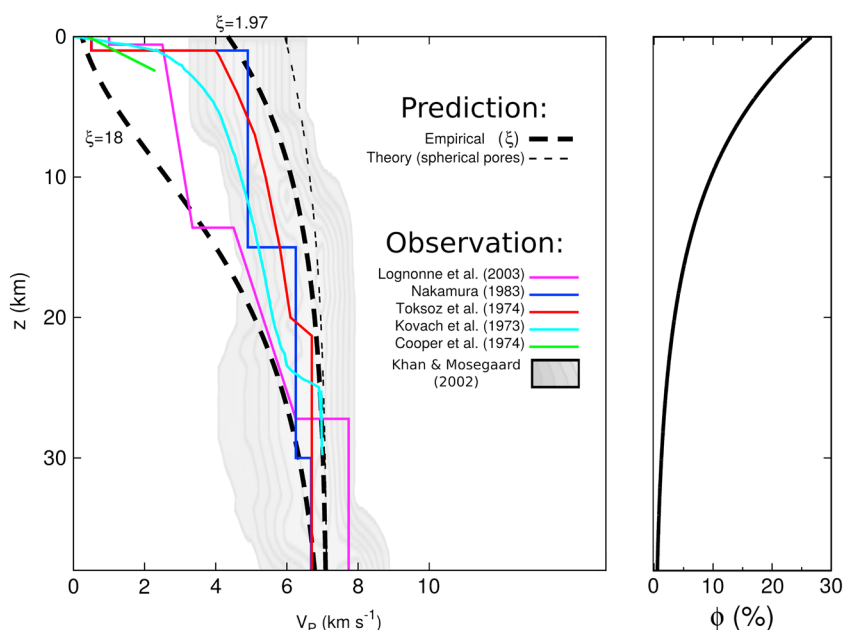
Figure 4. Comparison between porosity-predicted compressional seismic velocity profiles $V_P(z)$ below the Apollo 12–14 region and various seismically determined velocity profiles. Thick dashed lines depict the predicted profiles obtained with an empirical velocity-porosity law for lunar anorthosites [*Sondergeld et al.*, 1979] for our best fit density profile ($d = 9.8$ km, $\Delta\rho = 786$ kg m^{-3}; corresponding porosity profile $\phi(z)$ is displayed in the right). Two end-member values of the empirical parameter ξ were used: $\xi = 18$—relevant to highly fractured lunar anorthosites, with long, elongated cracks—and $\xi = 1.97$—relevant for spherical pores [*Sondergeld et al.*, 1979]. The thin dashed line depicts the result obtained using a theoretical model for spherical pores [*Smith*, 1974; *Christensen*, 1979], which resembles numerically derived results [*Mogilevskaya et al.*, 2007]. Six different lunar seismic models are displayed (see section S7 in the supporting information): in green, an early, shallow model [*Cooper et al.*, 1974] depicted as a linear trend excluding the biased [*Nakamura*, 2011] Apollo 17 Lunar Module impact data; in cyan, a pre-Apollo 17 era crustal model [*Kovach and Watkins*, 1973]; in red and blue, post-Apollo era models [*Toksöz et al.*, 1974; *Nakamura*, 1983]. Two more recent models are also included, in pink [*Lognonné et al.*, 2003] and in pale gray scale [*Khan and Mosegaard*, 2002]. The latter is a Bayesian model and displays contour lines defining equal-sized probability density intervals for the velocity distribution [*Khan and Mosegaard*, 2002].

and should not be affected by likely lateral variations in crustal thickness (see sections S3 and S6 in the supporting information).

4. Discussion and Conclusion

The SP-A region appears to possess a thinner low-density (porous) layer than the rest of the farside. This could be the result of: impact-induced removal (i.e., excavation) of preexisting fractured material; annealing of preexisting fractures [*Besserer et al.*, 2013; *Wieczorek et al.*, 2013a] within SP-A; generation of a thick, pore-free impact melt sheet [*Potter et al.*, 2012; *Vaughan et al.*, 2013] within SP-A; intrusive magmatic processes; redistribution of thick (porous) SP-A ejecta deposits over the rest of the farside; or a combination of these factors. The SP-A impact may have caused widespread deposition of up to a few kilometers of ejecta [*Petro and Pieters*, 2008; *Wieczorek et al.*, 2012]. Azimuthal averages of both the estimated bulk porosity and the depth scale d (Figure S11) exhibit an appreciable increase at a radial distance of ~1000 km from the center of SP-A, suggestive of the farside's shallow crustal structure being at least partially made of SP-A basin ejecta.

Seismic velocity profiles provide our only in situ deep lunar data. They are, however, restricted to the nearside of the Moon, in particular at the Apollo landing sites that are within or adjacent to the maria [*Wieczorek et al.*, 2006; *Khan et al.*, 2013]. Figure 4 compares various seismic *P* wave velocity determinations with synthetic velocity profiles based on our model exponential density profiles below a region near the Apollo 12–14 landing sites (cf. Figures 1–2). The synthetic profiles assume density variations are due only to porosity and use an experimentally constrained velocity-porosity law [*Sondergeld et al.*, 1979] for lunar fractured anorthosites, and also a purely theoretical prediction for spherical pores [*Smith*, 1974; *Christensen*, 1979]

(see section S7 in the supporting information). In the very shallow, highly porous region, the synthetic profile obtained assuming highly fractured anorthosites agrees well with most seismic models, whereas the synthetics assuming spherical pores provide a good match in deeper regions. Similar velocity predictions have recently been obtained by *Schmerr and Han* [2014] using a different approach. This figure highlights the potential power of high-degree gravity data to help refine future lunar seismic models [*Schmerr and Han*, 2014; *Weber and Schmerr*, 2014].

Mapping the spatial distribution of shallow porosity, as we have attempted here, will allow comparison with other data sets (e.g., surface composition). For instance, a recent reexamination of lunar craters' depth-diameter scaling laws has shown that craters on the highlands are systematically deeper than those on the mare [*Kalynn et al.*, 2013], probably owing to the highly fractured nature of the material forming the highlands. Crater morphology may thus provide a test of the density variations we have inferred here. Remotely acquired data such as those provided by GRAIL will probably remain one of the best ways for investigating the subsurface of planets and satellites for the next decades.

References

Antonenko, I., J. W. Head, J. F. Mustard, and B. Ray Hawke (1995), Criteria for the detection of lunar cryptomaria, *Earth Moon Planets*, *69*, 141–172, doi:10.1007/BF00613096.

Besserer, J., F. Nimmo, M. A. Wieczorek, W. S. Kiefer, J. C. Andrews-Hanna, and M. T. Zuber (2013), Theoretical and observational constraints on lunar mega-regolith thickness, *Proc. Lunar Planet. Sci. Conf.*, *44*, 2463.

Christensen, R. M. (1979), *Mechanics of Composite Materials*, 348 pp., Wiley-Interscience, New York.

Cooper, M. R., R. L. Kovach, and J. S. Watkins (1974), Lunar near-surface structure, *Rev. Geophys. Space Phys.*, *12*, 291–308, doi:10.1029/RG012i003p00291.

Dahlen, F. A., and F. J. Simons (2008), Spectral estimation on a sphere in geophysics and cosmology, *Geophys. J. Int.*, *174*, 774–807, doi:10.1111/j.1365-246X.2008.03854.x.

Garrick-Bethell, I., and M. T. Zuber (2009), Elliptical structure of the lunar South Pole-Aitken basin, *Icarus*, *204*, 399–408, doi:10.1016/j.icarus.2009.05.032.

Goossens, S., et al. (2011), Lunar gravity field determination using SELENE same-beam differential VLBI tracking data, *J. Geod.*, *85*, 205–228, doi:10.1007/s00190-010-0430-2.

Han, S.-C. (2013), Determination and localized analysis of intersatellite line of sight gravity difference: Results from the GRAIL primary mission, *J. Geophys. Res. Planets*, *118*, 2323–2337, doi:10.1002/2013JE004402.

Han, S.-C., N. Schmerr, G. Neumann, and S. Holmes (2014), Global characteristics of porosity and density stratification within the lunar crust from GRAIL gravity and LOLA topography data, *Geophys. Res. Lett.*, *41*, 1882–1889, doi:10.1002/2014GL059378.

Huang, Q., and M. A. Wieczorek (2012), Density and porosity of the lunar crust from gravity and topography, *J. Geophys. Res.*, *117*, E05003, doi:10.1029/2012JE004062.

Kalynn, J., C. L. Johnson, G. R. Osinski, and O. Barnouin (2013), Topographic characterization of lunar complex craters, *Geophys. Res. Lett.*, *40*, 38–42, doi:10.1029/2012GL053608.

Khan, A., and K. Mosegaard (2002), An inquiry into the lunar interior: A nonlinear inversion of the Apollo lunar seismic data, *J. Geophys. Res.*, *107*, 5036, doi:10.1029/2001JE001658.

Khan, A., A. Pommier, G. A. Neumann, and K. Mosegaard (2013), The lunar moho and the internal structure of the Moon: A geophysical perspective, *Tectonophysics*, *609*, 331–352, doi:10.1016/j.tecto.2013.02.024.

Kiefer, W. S., R. J. Macke, D. T. Britt, A. J. Irving, and G. J. Consolmagno (2012), The density and porosity of lunar rocks, *Geophys. Res. Lett.*, *39*, L07201, doi:10.1029/2012GL051319.

Konopliv, A. S., A. B. Binder, L. L. Hood, A. B. Kucinskas, W. L. Sjogren, and J. G. Williams (1998), Improved gravity field of the Moon from Lunar Prospector, *Science*, *281*, 1476–1480, doi:10.1126/science.281.5382.1476.

Konopliv, A. S., et al. (2013), The JPL lunar gravity field to spherical harmonic degree 660 from the GRAIL Primary Mission, *J. Geophys. Res. Planets*, *118*, 1415–1434, doi:10.1002/jgre.20097.

Konopliv, A. S., et al. (2014), High resolution lunar gravity fields from the GRAIL Primary and Extended Mission, *Geophys. Res. Lett.*, *41*, 1452–1458, doi:10.1002/2013GL059066.

Kovach, R. L., and J. S. Watkins (1973), The velocity structure of the lunar crust, *Moon*, *7*, 63–75, doi:10.1007/BF00578808.

Laneuville, M., M. A. Wieczorek, D. Breuer, and N. Tosi (2013), Asymmetric thermal evolution of the Moon, *J. Geophys. Res. Planets*, *118*, 1435–1452, doi:10.1002/jgre.20103.

Langseth, M. G., S. J. Keihm, and K. Peters (1976), Revised lunar heat-flow values, *Proc. Lunar Planet. Sci. Conf., 7*, 3143–3171.

Lemoine, F. G., et al. (2013), High-degree gravity models from GRAIL primary mission data, *J. Geophys. Res. Planets*, *118*, 1676–1698, doi:10.1002/jgre.20118.

Lemoine, F. G., et al. (2014), GRGM900C: A degree 900 lunar gravity model from GRAIL primary and extended mission data, *Geophys. Res. Lett.*, *41*, 3382–3389, doi:10.1002/2014GL060027.

Lewis, K. W., and F. J. Simons (2012), Local spectral variability and the origin of the Martian crustal magnetic field, *Geophys. Res. Lett.*, *39*, L18201, doi:10.1029/2012GL052708.

Lognonné, P., J. Gagnepain-Beyneix, and H. Chenet (2003), A new seismic model of the Moon: Implications for structure, thermal evolution and formation of the Moon, *Earth Planet. Sci. Lett.*, *211*, 27–44, doi:10.1016/S0012-821X(03)00172-9.

Mazarico, E., D. D. Rowlands, G. A. Neumann, D. E. Smith, M. H. Torrence, F. G. Lemoine, and M. T. Zuber (2012), Orbit determination of the Lunar Reconnaissance Orbiter, *J. Geod.*, *86*, 193–207, doi:10.1007/s00190-011-0509-4.

Mogilevskaya, S. G., J. Wang, and S. L. Crouch (2007), Numerical evaluation of the effective elastic moduli of rocks, *Int. J. Rock Mech. Min. Sci.*, *44*, 425–436, doi:10.1016/j.ijrmms.2006.09.004.

Nakamura, Y. (1983), Seismic velocity structure of the lunar mantle, *J. Geophys. Res.*, *88*, 677–686, doi:10.1029/JB088iB01p00677.

Nakamura, Y. (2011), Timing problem with the Lunar Module impact data as recorded by the LSPE and corrected near-surface structure at the Apollo 17 landing site, *J. Geophys. Res.*, *116*, E12005, doi:10.1029/2011JE003972.

Petro, N. E., and C. M. Pieters (2008), The lunar-wide effects of basin ejecta distribution on the early megaregolith, *Meteorit. Planet. Sci.*, *43*, 1517–1529, doi:10.1111/j.1945-5100.2008.tb01025.x.

Potter, R. W. K., G. S. Collins, W. S. Kiefer, P. J. McGovern, and D. A. Kring (2012), Constraining the size of the South Pole-Aitken basin impact, *Icarus*, *220*, 730–743, doi:10.1016/j.icarus.2012.05.032.

Rasmussen, K. L., and P. H. Warren (1985), Megaregolith thickness, heat flow, and the bulk composition of the moon, *Nature*, *313*, 121–124, doi:10.1038/313121a0.

Schmerr, N. C., and S.-C. Han (2014), Seismic and gravity modeling of the lunar megaregolith, *Proc. Lunar Planet. Sci. Conf., 45*, 2632.

Siegler, M. A., and S. E. Smrekar (2014), Lunar heat flow: Regional prospective of the Apollo landing sites, *J. Geophys. Res. Planets*, *119*, 47–63, doi:10.1002/2013JE004453.

Simons, F. J., F. A. Dahlen, and M. A. Wieczorek (2006), Spatiospectral concentration on a sphere, *SIAM Rev., 48*, 504–536, doi:10.1137/S0036144504445765.

Smith, D. E., et al. (2010), Initial observations from the Lunar Orbiter Laser Altimeter (LOLA), *Geophys. Res. Lett.*, *37*, L18204, doi:10.1029/2010GL043751.

Smith, J. C. (1974), Correction and extension of van der Poel's method for calculating the shear modulus of a particulate composite, *J. Res. Natl. Inst. Stand. A, 78A*, 355–361.

Sondergeld, C. H., L. A. Granryd, and H. A. Spetzler (1979), Compressional velocity measurements for a highly fractured lunar anorthosite, *Lunar Planet. Inst. Tech. Rep., 10*, 2147–2154.

Toksöz, M. N., A. M. Dainty, S. C. Solomon, and K. R. Anderson (1974), Structure of the Moon, *Rev. Geophys. Space Phys., 12*, 539–567.

Vaughan, W. M., J. W. Head, L. Wilson, and P. C. Hess (2013), Geology and petrology of enormous volumes of impact melt on the Moon: A case study of the Orientale basin impact melt sea, *Icarus*, *223*, 749–765, doi:10.1016/j.icarus.2013.01.017.

Weber, R. C., and N. C. Schmerr (2014), GRAIL refinements to lunar seismic structure, *Proc. Lunar Planet. Sci. Conf., 45*, 2008.

Wieczorek, M. A., and F. J. Simons (2005), Localized spectral analysis on the sphere, *Geophys. J. Int., 162*, 655–675, doi:10.1111/j.1365-246X.2005.02687.x.

Wieczorek, M. A., and F. J. Simons (2007), Minimum-variance multitaper spectral estimation on the sphere, *J. Fourier Anal. Appl., 13*(6), 665–692, doi:10.1007/s00041-006-6904-1.

Wieczorek, M. A., et al. (2006), The constitution and structure of the lunar interior, *Rev. Min. Geoch., 60*, 221–364.

Wieczorek, M. A., B. P. Weiss, and S. T. Stewart (2012), An impactor origin for lunar magnetic anomalies, *Science, 335*, 1212–1215, doi:10.1126/science.1214773.

Wieczorek, M. A., et al. (2013a), The crust of the Moon as seen by GRAIL, *Science, 339*, 671–675, doi:10.1126/science.1231530.

Wieczorek, M. A., et al. (2013b), High-resolution estimates of lunar crustal density and porosity from the GRAIL Extended Mission, *Proc. Lunar Planet. Sci. Conf., 44*, 1914.

Ziethe, R., K. Seiferlin, and H. Hiesinger (2009), Duration and extent of lunar volcanism: Comparison of 3D convection models to mare basalt ages, *Planet. Space Sci., 57*, 784–796, doi:10.1016/j.pss.2009.02.002.

Zuber, M. T., and C. T. Russell (2014), *GRAIL: Mapping the Moon's Interior*, 76 pp., Springer, New York.

Zuber, M. T., D. E. Smith, F. G. Lemoine, and G. A. Neumann (1994), The shape and internal structure of the Moon from the clementine mission, *Science, 266*, 1839–1843, doi:10.1126/science.266.5192.1839.

Zuber, M. T., et al. (2013), Gravity field of the Moon from the Gravity Recovery and Interior Laboratory (GRAIL) mission, *Science, 339*, 668–671, doi:10.1126/science.1231507.